Int J Adv Manuf Technol (2017) 92:2207–2216
DOI 10.1007/s00170-017-0234-0

ORIGINAL ARTICLE

Water cooling keyhole gas tungsten arc welding of HSLA steel

Wenfei Fan[1] · Sansan Ao[1,2] · Yifei Huang[1] · Weidong Liu[1] · Yang Li[1] · Yueqiao Feng[1] · Zhen Luo[1,2,3] · Ben Wu[4]

Received: 23 August 2016 / Accepted: 1 March 2017 / Published online: 30 March 2017

Abstract Keyhole gas tungsten arc (K-TIG) welding with water cooling system was used to weld high-strength low-alloy steel of mid-thickness (thickness ranging 6–13 mm). Q345 plates of 8-mm thickness were jointed in a single pass without filler metal. The weld properties, including mechanical properties and microstructure, were analyzed. The maximum tensile strength of the weld was similar with that of the base metal, while the elongation and impact property of the weldment were decreased compared with the base metal. The numerical simulation result revealed that water cooling method used in K-TIG welding is greatly helpful in reducing the volume of the welding pool due to the enhanced cooling effect. Additionally, improved holding power of the welding pool can be obtained due to the increased surface tension.

Keywords Keyhole gas tungsten arc welding · Water cooling · HSLA Q345 · Numerical simulation · Mechanical properties · Microstructures

✉ Sansan Ao
ao33@tju.edu.cn

✉ Zhen Luo
lz@tju.edu.cn

[1] School of Materials Science and Engineering, Tianjin University, Tianjin 300072, China

[2] Tianjin University, 31-291, No. 135 Yaguan Road, Tianjin 300350, China

[3] Collaborative Innovation Center of Advanced Ship and Deep-Sea Exploration, Shanghai 200240, China

[4] Harbin Huade University, Harbin 150025, China

1 Introduction

Keyhole gas tungsten arc (K-TIG) welding is invented by Australian research organization CSIRO in 1997. During K-TIG welding processing, the welding current was increased to higher than 300 A to boost the arc force. Strong arc force was balanced by the surface tension of the welding pool, so that a keyhole can be formed during welding and the weld depth can be increased. Good appearance of the front-side and back-side of weld can be achieved in a single pass at a relatively high welding speed (>250 mm min^{-1}). Lathabai et al. studied the K-TIG welding of commercially pure (CP) titanium [1]. Their results showed that 12.7-mm-thick CP titanium can be welded in a single pass at a welding speed of 250 mm min^{-1}. They found that compared with the traditional TIG weld, the tensile properties, hardness, and toughness of the K-TIG weld were similar but the productivity of K-TIG welding was increased appreciably. Furthermore, Lathabai et al. also applied K-TIG welding to CP zirconium [2]. In their study, 6.35-mm-thick CP zirconium plates were welded in a single pass at a welding speed of 500 mm min^{-1}, and the ductility of joints was high. The microstructure of K-TIG welds showed no porosity or other defects. Feng et al. successfully applied the K-TIG to weld 10-mm-thick AISI 316-L stainless steels without filler wire or edge preparation [3]. In one word, K-TIG welding has great potential in joining mid-thickness (thickness ranging 6–13 mm) workpieces in industry because of its high efficiency and low cost [4].

To sustain a stable keyhole, the following equation should be satisfied [5]:

$$wh < \gamma \Big/ \rho g \tag{1}$$

where w is the root bead width, h is the plate thickness, γ is the surface tension, ρ is the density, and g is the acceleration due to gravity. Rosenthal indicated that the width of the root bead

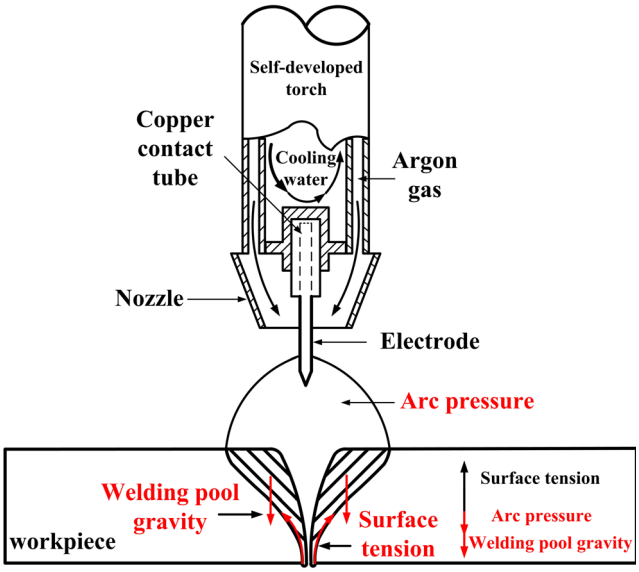

Fig. 1 Force analysis during K-TIG welding

decreased with the thermal conductivity decreasing [6]. Accordingly, materials with low thermal conductivity or large surface tension are easier to be welded by K-TIG welding. And as shown in Fig. 1, the stable keyhole of K-TIG welding is a dynamic balance of the downward forces and upward forces. The downward forces are mainly arc pressure and welding pool gravity. The upward force is mainly surface tension.

Most current researches focus on the welding of materials with low thermal conductivity such as CP titanium, CP zirconium, and stainless steel, of which the thermal conductivity is about 16.2 W/m h [7, 8]. It is difficult to weld materials with relatively high thermal conductivity such as high-strength steel, of which the thermal conductivity is about 48 W/m h [9]. In order to apply the K-TIG welding to high strength steel, one possible approach is to increase the surface tension of welding pool, according to Eq. 1. Since the surface tension is inverse proportional to the temperature [10], lower the temperature by water cooling is an efficient method to increase the surface tension.

In the fusion-welding processing, cooling methods with different cooling medium are adopted. A new laser-welding process with the local cooling was presented and applied to two automotive dual-phase steels, DP780 and DP980, by Wei et al. [11]. It is observed that the local cooling during laser-welding process can greatly reduce the martensite tempering and thus reduce the heat-affected zone softening. Manikandan SGK et al. have investigated the interdendritic Laves phase and the microsegregation in alloy 718 fusion zone cooled with liquid nitrogen during welding [12]. Conventional GTA welding process was employed with modified waveform and two types of shielding gas and filler metal. It was found that the enhanced cooling rate with liquid nitrogen reduced the interdendritic phases, which were confirmed in both the electron microscopic and the X-ray diffraction analyses. Hamatani H et al. have carried out using the cooling conductor liquid nitrogen to minimize the ultra-fine-grained steel (UFGS)'s heat-affected zone (HAZ) size during the laser welding [13]. It was found that a shielding gas, with adequate flow rate for the liquid nitrogen depth, was used to remove nitrogen from the area of laser beam irradiation to stabilize the weld bead. Moreover, cooling methods are also used in solid phase joining. Zhang et al. applied water cooling to control the temperature level and improve the mechanical properties of friction stir weld [14]. Mofid et al. investigated the effect of water cooling upon dissimilar friction stir welding of Al alloy to Mg alloy and pointed out that water cooling promoted the formation of fine grain and alleviated the formation of intermetallic phases [15].

High-strength low-alloy (HSLA) steel has been widely used in the manufacturing of vehicles, ships, oil and gas transmission lines, offshore oil-drilling platforms, pressure vessels, and so on, because of its high strength-to-weight ratio, excellent ductility, and good weldability [16, 17]. The Q345 steel is a common (HSLA) steel with excellent mechanical properties and is widely used for petrochemical plants and nuclear industry [18]. The common technology for mid-thick Q345 steel plates is multipass welding, which is complex and inefficient. Therefore, it is necessary to apply a new technology to the mid-thick Q345steel plate welding. In present paper, a water cooling K-TIG welding is applied to 8-mm-thick Q345 steel plates in a flat position. The microstructure and mechanical properties of the joints were analyzed. Numerical simulation was also employed to quantitatively understand the dynamics of the keyhole and molten pool.

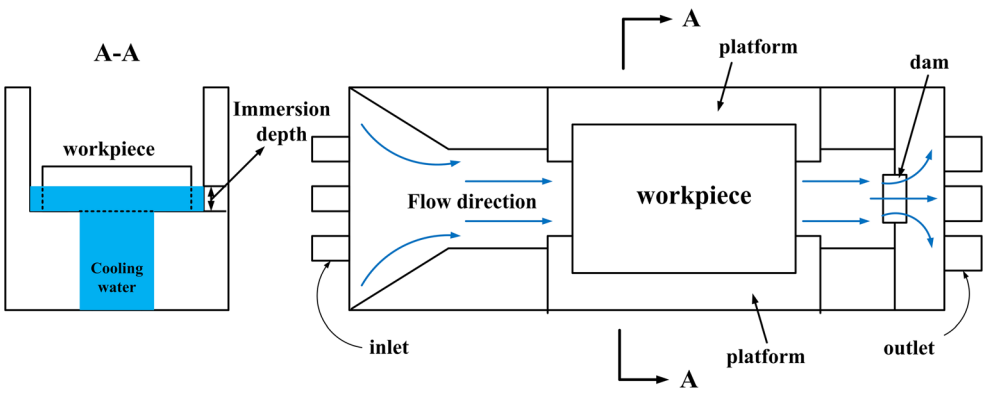

Fig. 2 Schematic of water cooling system

A novel heat dissipation method with water cooling is used to improve the weld formation of Q345.

To our knowledge, it is the first time that a heat dissipation method was used to solve the formation of weld in K-TIG. Numerical simulation is also used to analyze the heat transformation in the process of K-TIG.

2 Experimental procedures

2.1 Methods

A self-developed K-TIG torch (as shown in Fig. 1) fitted with a 350-mm-long trailing shield and water cooling system was used in this research. The entire torch barrel was cooled by the circulating water so that it could stand the large welding current (up to 1000 A). The tungsten electrode was cooled by a copper contact tube to increase the current density and reduce the electrode loss [19].

The water cooling system was composed of welding platform and circulating water canal, as shown in Fig. 2. The welding platform, which connected with the power source, was made by stainless steel sheet. The shape of the canal inlet was flared, which turns the water from turbulence into laminar motion. The preliminary experiments showed that with same flow rate, the water in laminar motion has better cooling effect than the water in turbulence. At the outlet of the system, a dam was set to adjust the immersion depth of the specimen. The circulating water was pumped up by the adjustable pump; the fluid flow speed of the water in the canal could also be controlled.

The torch was operated with DC electrode negative polarity and powered by a Miller 1250 power supply. During welding, the torch was fixed in position by the *Y-Z* axis holder and the welding speed was controlled by the *X* axis platform under the water cooling system. The diameter of the ceria-doped tungsten electrode was 6.0 mm and the vertex angle was 60°. The shielding gas was pure argon. And the parameters concluded from the pre-experiments are shown in Table 1, which were used to numerical simulation and mechanical test.

2.2 Material

The material used was Q345 plate with dimensions of 250 × 150 × 8 mm. The chemical composition of the material is presented in Table 2. The ultimate tensile strength, yield tensile strength, and elongation of the used material were 345 MPa, 500 MPa, and 21%, respectively. The microstructure of the base metal consisted of uniform banded ferrite and a small amount of black pearlite, as shown in Fig. 3.

Table 1 Parameters in the water cooling K-TIG

Welding current (A)	Welding speed (mm/min)	Arc length (mm)	Gas flow rate (L/min)	Cooling water flow rate (L/min)
480	240	2.5	25	50

Table 2 Chemical composition of Q345 (wt%)

C	Si	Mn	P	S	Cr	Mo	Ni	V	Nb
0.17	0.35	1.48	0.21	0.08	0.25	0.08	0.45	0.12	0.015

2.3 Joint characterization

Optical microscopy was used to characterize the weld. Samples were etched with 4% Nital solution to reveal the microstructure. Transverse tensile tests were performed in accordance with CB/T 2651–2008 [20], and Charpy V-notch impact tests were conducted in accordance with GB/T 2650–2008 [21]; the energy absorbed in fracture was recorded. The specimen dimensions are shown in Fig. 4. After the tensile test, the facture morphology was observed with a scanning electron microscope (SEM). Vickers microhardness test was carried out to measure the hardness distribution across the welded joint with a load of 1 kg.

3 Numerical simulation

A three-dimensional finite element model from software ANSYS was used to investigate the effect of cooling on the weld formation [22, 23]. Figure 5 shows the dimensions and element grid of the finite element model. Half of the workpiece, which is perpendicular to the welding direction, was modeled to analysis for the symmetry of the butt joint. Element type solid70 was employed and the finite element model consisted of 79,097 nodes. The small element size has been used in the fusion zone and heat-affected zone of

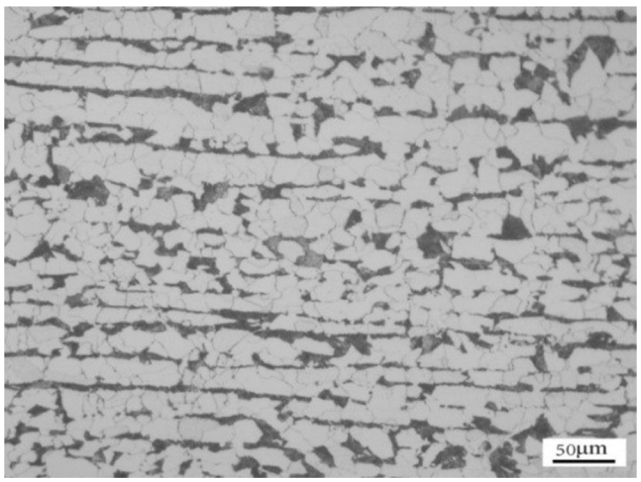

Fig. 3 Microstructure of the base metal

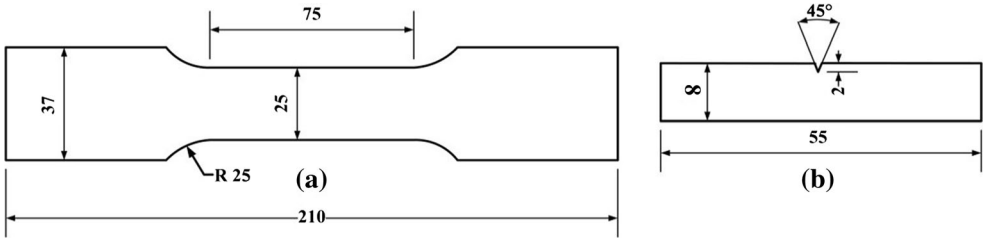

Fig. 4 Test specimen dimensions. **a** Tensile test specimen. **b** Charpy V-notch impact test specimen

model in order to account for the high-temperature gradient. The thermo-physical properties of the material were obtained from references [24, 25].

The governing equation for the transient temperature field is listed as follows:

$$\frac{\partial}{\partial x}\left(k\frac{\partial T}{\partial x}\right)+\frac{\partial}{\partial y}\left(k\frac{\partial T}{\partial y}\right)+\frac{\partial}{\partial z}\left(k\frac{\partial T}{\partial z}\right)+q_v=\rho C_P\frac{\partial T}{\partial t} \quad (2)$$

where T is the temperature; t is the time; q_v is the internal heat generation rate per unit volume; and ρ, C_P, and k are the density, specific heat, and thermal conductivity, respectively.

Two heat sources which include double ellipsoidal and cylindrical were employed according to references [26, 27]. The mathematical equation that describes the heat source models are given in Eqs. (3) and (4).

$$q_1(x,y,z)=q_m e^{-3x^2/a_1^2}e^{-3y^2/b^2}e^{-3z^2/c^2} \quad (3)$$

$$q_2(x,y,z)=q_m e^{-3x^2/a_2^2}e^{-3y^2/b^2}e^{-3z^2/c^2} \quad (4)$$

where q_m represents the maximum heat source intensity and given by

$$q_m=\frac{6\sqrt{3}f_1Q}{\pi\sqrt{\pi}a_1bc}=\frac{6\sqrt{3}f_2Q}{\pi\sqrt{\pi}a_2bc} \quad (5)$$

where $f_1+f_2=2$ and $f_1=2a_1/(a_1+a_2)$, $f_2=2a_2/(a_1+a_2)$, a_1, a_2, b, and c are chosen from the actual bead dimensions. $Q=\eta UI$ is the total heat input, and η is the power allocation ratio, which is about 0.8.

The diameter of power density of the cylindrical heat source model is Gaussian distribution and uniform distribution on the depth direction of the cylindrical heat source, which is given by

$$q(r,z)=q_m\cdot D(z)\cdot\exp\left(-\frac{3r^2}{{r_0}^2}\right) \quad (6)$$

where r_0 is the radii of the cylindrical and $D(z)$ and the maximum heat intensity q_m are given by

$$D(z)=\frac{mz+r_0}{r_0} \quad (7)$$

$$q_m=\frac{6Q}{\pi r_0 h(mz+2r_0)} \quad (8)$$

where m is the pondage factor and h is the heat source function depth.

The boundary conditions consist of water cooling and air cooling. In the air cooling condition, convective and radiation losses on the model surfaces were taken into account. The radiation was transferred into the convective to simplify the calculation [28]. In the water cooling condition, the cooling water was subcooled boiling. The coefficient of heat transfer was estimated by the heat transfer coefficient under without phase-change condition and boiling condition. Combined with the boiling intensity in welding, the coefficient was 15,000 W m^{-2} K^{-1}.

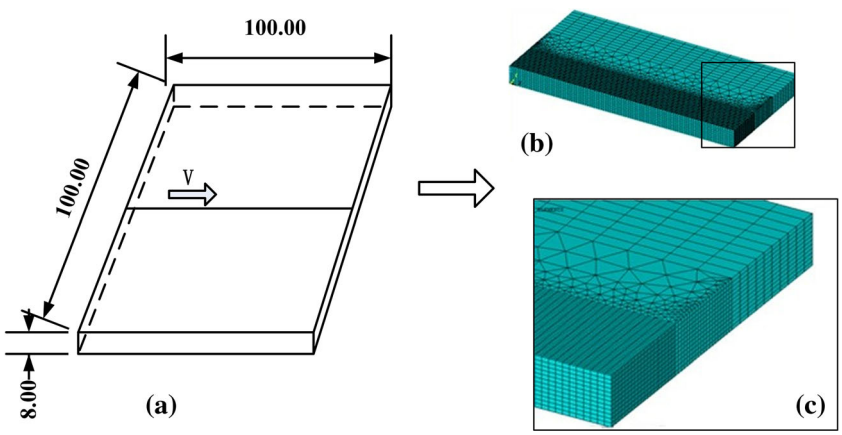

Fig. 5 Dimension of welding block and diagram of mesh model

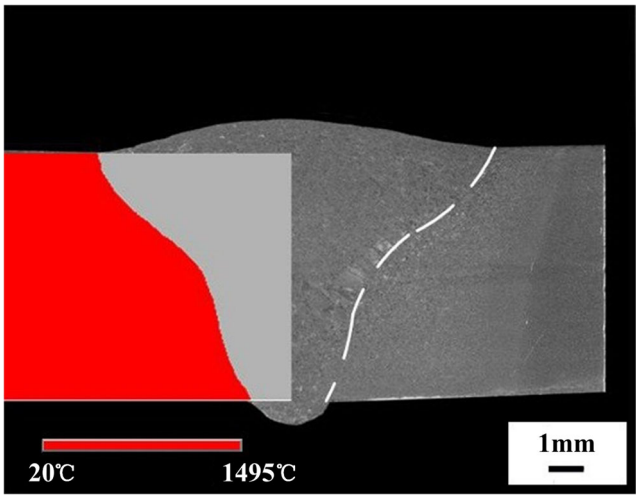

Fig. 6 Comparison of calculated and experimental weld profile

4 Results and discussion

4.1 Simulation results

Figure 6 is the comparison of calculated and experimental weld profiles under water cooling. The calculated result agreed well with the experimental one, indicating the validation of the model. The temperature field distributions on the workpiece surface under air and water cooling conditions are shown in Fig. 7. Obviously, lower temperature and smaller welding pool were obtained under the water cooling condition.

Figures 8 and 9 show the three-dimensional diagram and sectional view of weld metal and thermal cycle curve of the weld bead under air and water cooling conditions. The distance of *a*, *b*, *c*, and *d* to the middle of the weld root is 0, 1.5, 3, and 4.5 mm, respectively. The volume of the welding pool was too large in the air cooling condition, so the welding pool collapsed and keyhole could not be formed. Compared with the air cooling, the weld bead width decreased by 60% in the water cooling; therefore, the gravity of the welding pool decreased. It is easier to get balance by relatively small surface tension and to obtain a stable keyhole. Furthermore, the lower temperature at the weld bead leads to larger surface tension, which is benefit to hold the welding pool and to keep the keyhole stable.

4.2 Microstructure characteristics

Figure 10 shows the macro/microstructure of welded joint. A fully penetrated weld can be obtained in a single pass without filler metal. No obvious defects, such as porosity or cracking, are observed. It could be concluded that with keeping the surface dry, the hydrogen could be avoided at some degree, and the content of diffusion hydrogen could also be restricted. Therefore, the cold cracking susceptibility of the welds was low. As shown in Fig. 10a, an obvious arc-shaped boundary was formed in the middle of the welded joint marked as blue. The boundary was determined by the different cooling rate from the upper to lower part, which is affected by the immersion depth of the specimen.

The microstructure of welded joint was divided into fusion zone (FZ) and HAZ. Figure 10b shows the microstructure of weld root on fusion zone. Proeutectoid ferrite nucleated at the equiaxed austenite grain boundary and then grew inward. White granular ferrite and little widmanstatten structure were found because of the high-heat input of K-TIG welding. The fine grains are due to the high cooling rate of water cooling system. Some fine acicular ferrites were found in the black

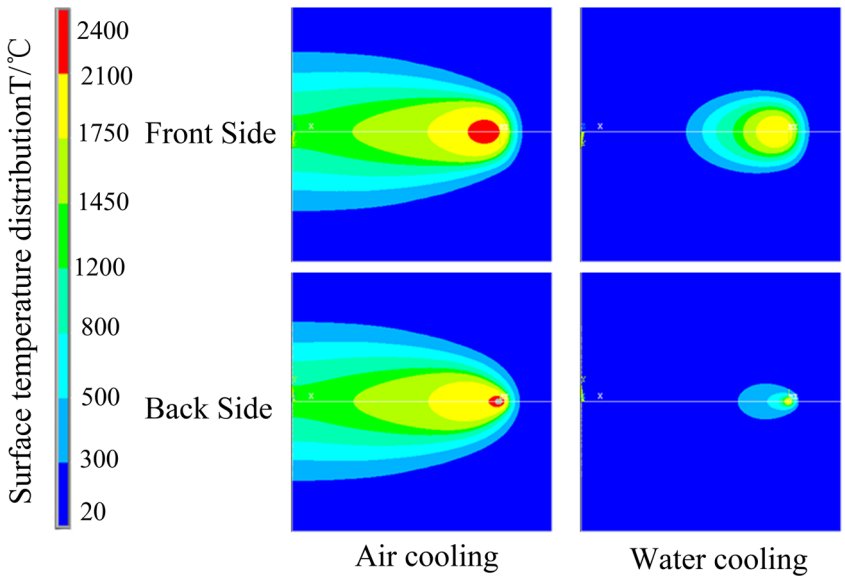

Fig. 7 Surface temperature field distribution of weldment

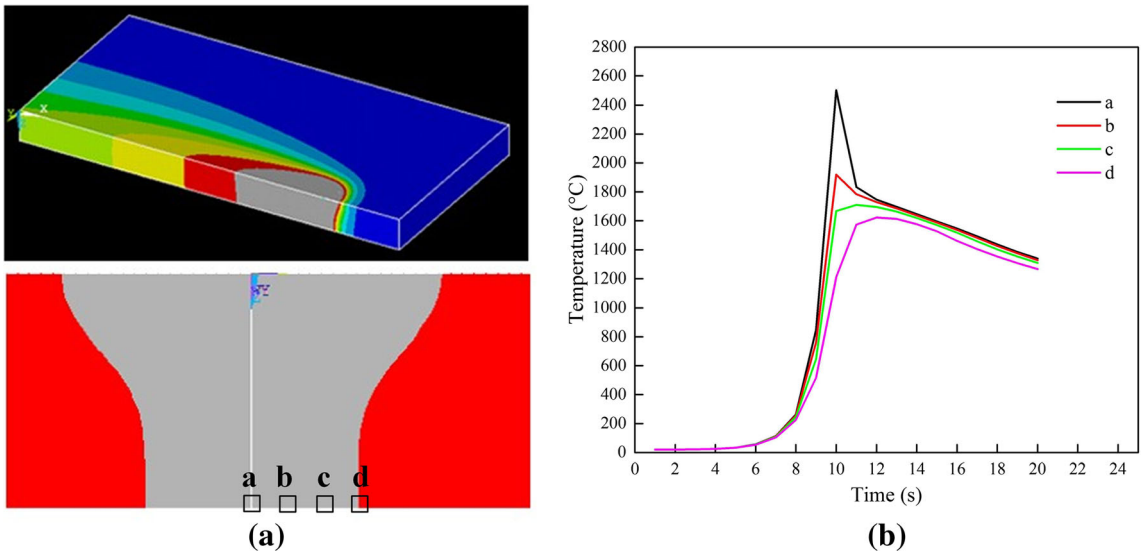

Fig. 8 Three-dimensional diagram and sectional view of weld metal and thermal cycle curve of the weld bead under air cooling condition

pearlite blocks. Based on the theory of welding metallurgy, with the high cooling rate, the transformation product will change to martensite. However, the high heat in the process of K-TIG removed that negative effect and decreased the high cooling rate. The microstructure of the fusion zone mid (Fig. 10c) is similar to the root. Nevertheless, the austenite, proeutectoid ferrite, granular ferrite, and widmanstatten structure grew obviously because of the decrease of cooling rate. In Fig. 10d, the arc boundary shown in the blue was affected by the cooling condition and mainly consisted of columnar crystals along the heat dissipation direction with low cooling rate according to the constituent supercooling theory. The proeutectoid ferrite distributed along the boundary of columnar crystal, as well as the acicular ferrite, widmnanstatten, and few upper bainite. Microstructure above the boundary is shown in Fig. 10e. With high-heat input and lower cooling rate, the first crystallized cellular grains were formed. And the cellular grains are stubby from the grain morphology.

Regions *f-i* marked in Fig. 10a belong to the HAZ. The grain size of HAZ gradually reduced from bottom to upper zone. Figure 10f shows the microstructure of a narrow section near the fusion line in HAZ. Obviously, columnar crystals formed because of the high temperature in this area. Fine granular ferrite precipitated along the columnar crystal boundary. There are also some acicular ferrites, and few widmanstatten structures existed in the grains. Away from the fusion line is the overheated zone, as shown in Fig. 10g. Proeutectoid ferrite nucleated at the equiaxed austenite and black pearlite matrix inside the austenite. Next to the overheated zone is the normalized zone. The microstructure in the

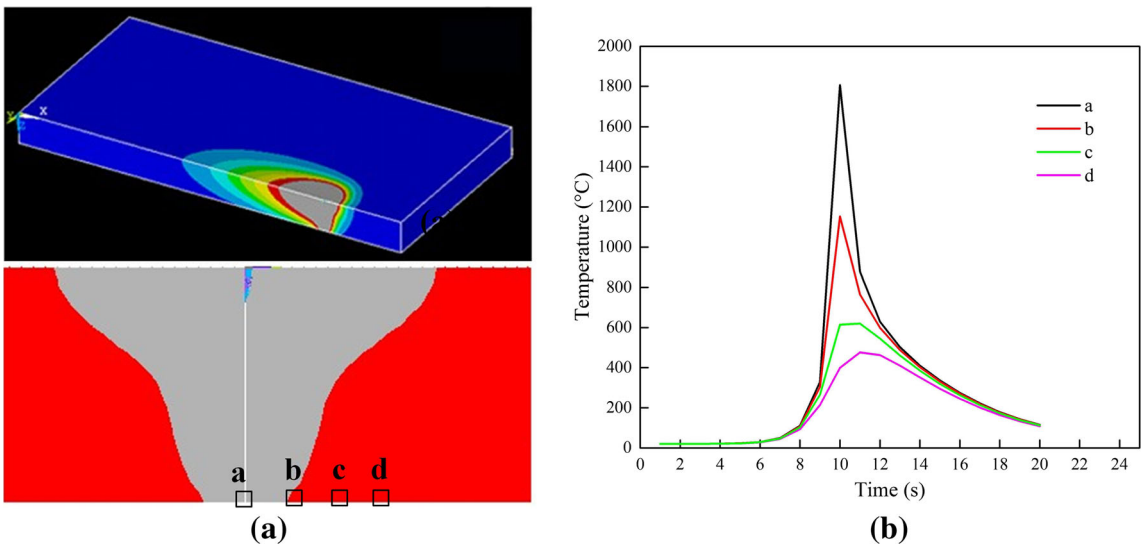

Fig. 9 Three-dimensional diagram and sectional view of weld metal and thermal cycle curve of the weld bead under water cooling condition

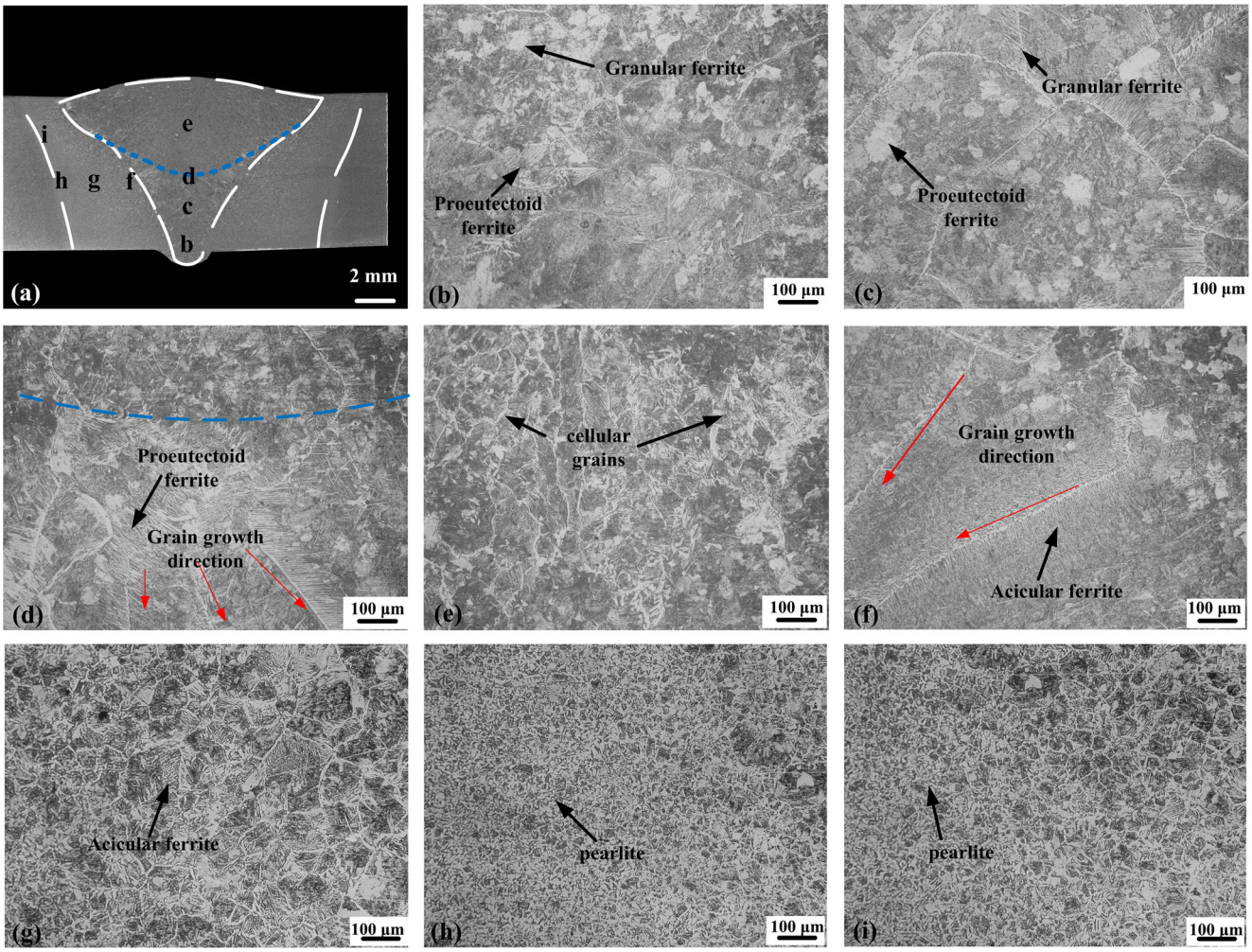

Fig. 10 Joint microstructure. **a** Transverse cross section. **b** Weld root. **c** Joint mid. **d** Microstructure around the boundary. **e** Microstructure above the boundary. **f** Section near the fusion line. **g** Overheated zone. **h**, **i** Normalized zone

normalized zone is shown in Fig. 10h, i, in which the main structure is the polyhedron ferrite grains and few pearlites.

The Vickers hardness of the weld is shown in Fig. 11. The blue line, red line, and black line represent the hardness test

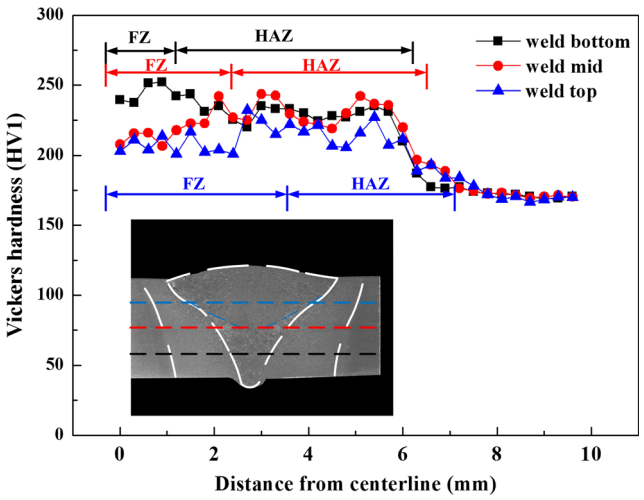

Fig. 11 Hardness distribution in the welded joint

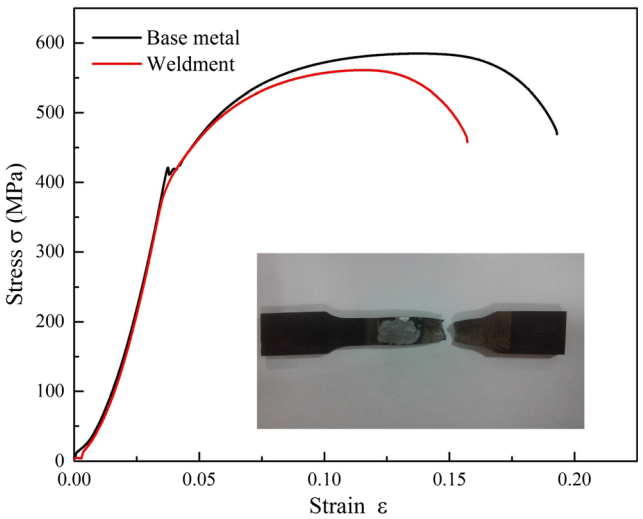

Fig. 12 Typical tensile curves of weldment and base metal

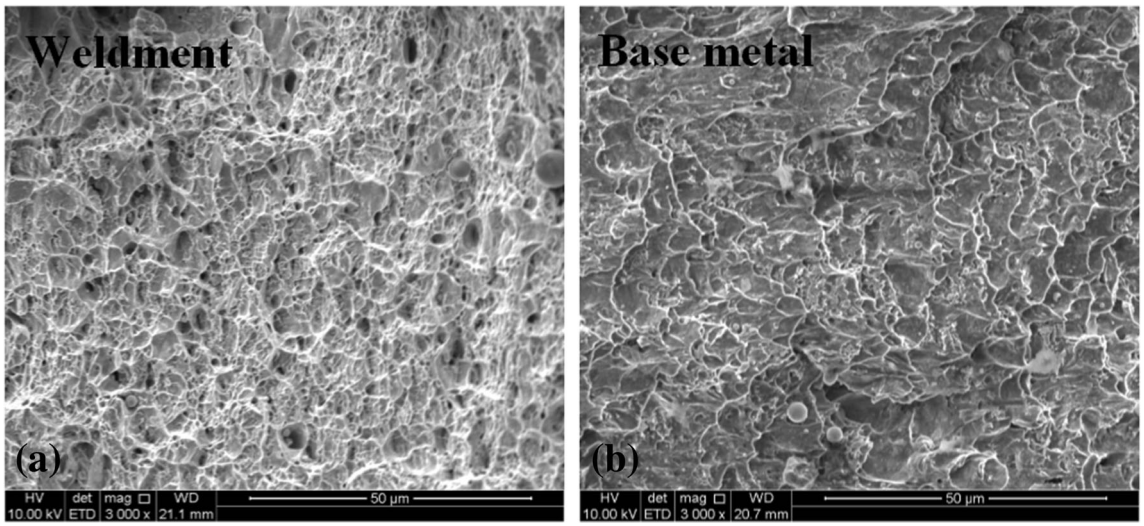

Fig. 13 Morphology of the tensile fracture surface. **a** Weldment. **b** Base meal

locations of 2 mm from the top surface, middle of the specimen, and 2 mm from the bottom side, respectively. Basically, the hardness of the FZ and HAZ is higher than that of the base metal. Under the function of the cooling water system, with the increase of the cooling rate, the hardness in FZ increased from top to bottom and the hardness of the bottom finally larger than that in HAZ. In HAZ, the hardness of mid and bottom are almost same and a little larger than that of the top corresponding to the microstructure in Fig. 10.

4.3 Mechanical properties

Figure 12 shows the typical tensile curves of weldment and base metal. High tensile strength can be achieved with water cooling K-TIG welding. Similar to most of other welding technologies, the fracture of Q345 weld often occurs at the base metal. The fracture of the weld made by underwater welding often occurs in weld due to the diffusion hydrogen [29]. However, in water cooling K-TIG welding, the surface of specimen is dry and the bottom of the weld is narrow. The diffusion hydrogen in the welded joint is, therefore, restricted, and therefore, the cold cracking is avoided effectively. Comparing the fracture surfaces of the base metal and weld (Fig. 13), it can be seen that they showed similar ductile fracture characteristics with dimples. This indicates that relatively high ductility and toughness of the welded joint can be achieved with water cooling K-TIG welding.

In the Charpy V-test, the average values of impact energy of the weld, HAZ, and base metal were 126, 130, and 140 J, respectively. The impact energy of weld is lower than that of base metal due to the formation of upper bainites during the water cooling K-TIG welding. The upper bainites have obvious grain orientation so that the fracture will propagate along the orientation with low energy. The fine grain size in HAZ contributed to its good impact property. According to the impact fracture surfaces (Fig. 14), it can be observed that the morphology of the impact fracture surfaces of base metal and HAZ shows typical characteristics of dimples, while the morphology of the impact fracture surface of weld shows cleavage character.

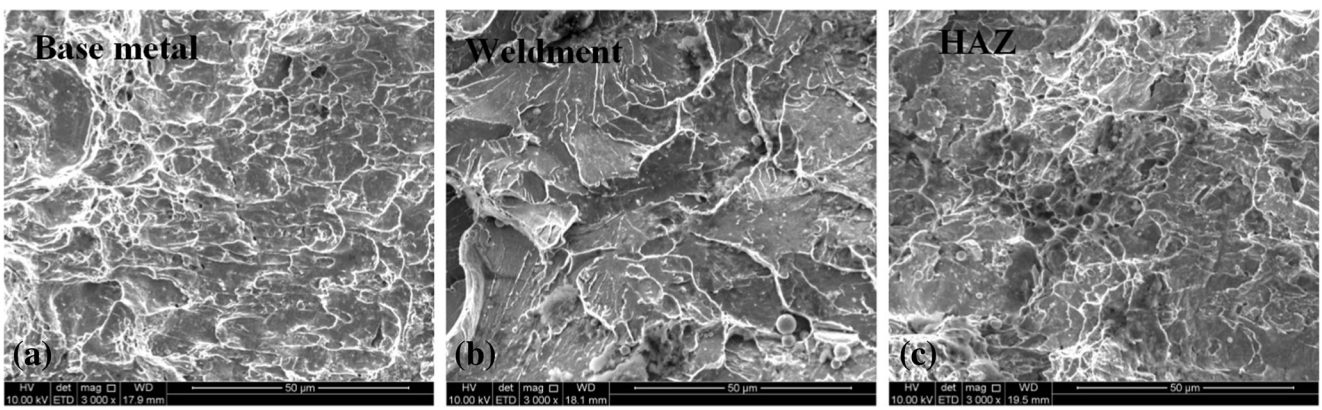

Fig. 14 Morphology of the impact fracture surface. **a** Base metal. **b** Weldment. **c** HAZ

5 Conclusions

In this paper, a novel water cooling K-TIG welding method is proposed to weld 8-mm-thick Q345 HSLA steel. Microstructure and mechanical properties of welded joint, including hardness, tensile strength, and impact property, were investigated. Several important conclusions can be drawn as follows.

(1) The 8-mm-thick Q345 steel can be successfully welded using water cooling K-TIG welding in single pass without filler. Water cooling K-TIG welding is greatly helpful in reducing the width of the weld root because of the enhanced cooling effect at the bottom. Additionally, improved holding effect of the welding pool can be obtained due to the increased surface tension.

(2) The shape of the weld showed typical "nail-shape," which indicates the enhanced stability of keyhole during the water cooling K-TIG welding. There is no defect, such as cold fracture and porosity, formed in the weld. The microstructures of the weld are complex and show obvious difference from the top surface to the bottom of the weld. The microstructures of the HAZ are uniform from the top to the bottom of HAZ.

(3) The tensile fracture occurred in the base metal, and the morphology of the fracture surface showed typical characteristics of dimple. The tensile strength was 560 MPa compared to the base metal tensile strength of 580 MPa, indicating good ductile and toughness. The average values of impact energy of the weld, HAZ, and base metal, respectively, were 126, 130, and 140 J, respectively, which indicates the good impact property of the joint.

Acknowledgements The authors gratefully acknowledge the support of the National Natural Science Foundation of China under Grant No. 51405335 and Grant No. 51575383 and the Provincial Science and Technology Program of Guangdong Province under Grant No. 2013B090600149.

References

1. Lathabai S, Jarvis BL, Barton KJ (2001) Comparison of keyhole and conventional gas tungsten arc welds in commercially pure titanium. Mater Sci Eng A 299:81–93. doi:10.1016/S0921-5093(00)01408-8
2. Lathabai S, Jarvis BL, Barton KJ (2008) Keyhole gas tungsten arc welding of commercially pure zirconium. Sci Technol Weld Join 13(6):573–581. doi:10.1179/136217108X329296
3. Feng YQ, Luo Z, Liu ZM, Li Y, Luo YC, Huang YX (2015) Keyhole gas tungsten arc welding of AISI 316L stainless steel. Mater Des 85:24–31. doi:10.1016/j.matdes.2015.07.011
4. Jarvis BL (2001) Keyhole gas tungsten arc welding: a new process variant. Dissertation, University of Wollongong
5. Rosenthal D (1941) Mathematical theory of heat distribution during welding and cutting. Weld J 20(5):220–234
6. Rosenthal R (1946) Theory of moving sources of heat and its applications to metal treatments. Trans ASME 68:849–866
7. Bai JY, Yang CL, Lin SB, Dong BL, Fan CL (2016) Mechanical properties of 2219-Al components produced by additive manufacturing with TIG. Int J Adv Manuf Technol 86(1–4):479–485. doi:10.1007/s00170-015-8168-x
8. Mostafapour A, Gholizadeh V (2014) Experimental investigation of the effect of vibration on mechanical properties of 304 stainless steel welded parts. Int J Adv Manuf Technol 70(5–8):1113–1124. doi:10.1007/s00170-013-5350-x
9. Jarvis BL, Ahmed NU (2000) Development of keyhole mode gas tungsten arc welding process. Sci Technol Weld Join 5(1):21–1718. doi:10.1179/136217100322910624
10. Li SL (2009) Physical chemistry. Beijing, China
11. Wei C, Zhang J, Yang S, Sun L, Tao W, Wu F, Xia W (2015) Improving formability of laser welded automotive dual phase steels with local cooling. Sci Technol Weld Join 20(2):145–154. doi:10.1179/1362171814Y.0000000263
12. Manikandan SGK, Sivakumar D, Rao KP, Kamaraj M (2014) Microstructural characterization of liquid nitrogen cooled alloy 718 fusion zone. J Mater Process Technol 214(12):3141–3149. doi:10.1016/j.jmatprotec.2014.07.022
13. Hamatani H, Miyazaki Y, Otani T, Ohkita S (2006) Minimization of heat-affected zone size in welded ultra-fine grained steel under cooling by liquid nitrogen during laser welding. Mater Sci Eng A 426(1–2):21–30. doi:10.1016/j.msea.2006.03.024
14. Zhang HJ, Liu HJ, Yu L (2012) Effect of water cooling on the performances of friction stir welding heat-affected zone. Journal of Mater Eng Performance 21(7):1182–1187. doi:10.1007/s11665-011-0060-8
15. Mofid MA, Abdollah-zadeh A, Malek GF (2012) The effect of water cooling during dissimilar friction stir welding of Al alloy to Mg alloy. Mater Des 36:161–167. doi:10.1016/j.matdes.2011.11.004
16. Nathana SR, Balasubramanian V, Malarvizhi S, Rao AG (2015) Effect of welding processes on mechanical and microstructural characteristics of high strength low alloy naval grade steel joints. Defence Technology 11:308–317. doi:10.1016/j.dt.2015.06.001
17. Hidetoshi F, Ling C, Nobuhiro T, Masakatsu M, Kazuhiro N, Kiyoshi N (2006) Friction stir welding of carbon steels. Mater Sci Eng A 429(1–2):429–507. doi:10.1016/j.msea.2006.04.118
18. Xiong Y, Hu XX (2012) The effect of microstructures on fatigue crack growth in Q345 steel welded joint. Fatigue Fract Eng Mater Struct 35:500–512. doi:10.1111/j.1460-2695.2011.01640.x
19. Lohse M, Füssel U, Schuster H, Friedel J, Schnick M (2013) Keyhole welding with CF-TIG (cathode focussed GTA). Weld World 57:735–741. doi:10.1007/s40194-013-0074-y
20. GB 2651 (2008) Tensile test methods on welded joints, general administration of quality supervision, inspection and quarantine of the People's Republic of China, China National Standardization Management Committee
21. GB 2650 (2008) Impact test methods on welded joints, general administration of quality supervision, inspection and quarantine of the People's Republic of China, China National Standardization Management Committee
22. Varghese VMJ, Suresh MR, Kumar DS (2013) Recent developments in modeling of heat transfer during TIG welding—a review. Int J Adv Manuf Technol 64(5–8):749–754. doi:10.1007/s00170-012-4048-9
23. Ranjbarnodeh E, Serajzadeh S, Kokabi AH, Hanke S, Fischer A (2011) Finite element modeling of the effect of heat input on residual stresses in dissimilar joints. Int J Adv Manuf Technol 55(5–8):649–656. doi:10.1007/s00170-010-3095-3
24. Zhao YB (2000) Practical manual pressure vessel materials: carbon and alloy steel. Beijing, China
25. Deng DA, Tong YG, Zhou ZY (2011) Numerical modeling of welding distortion in thin-walled mild steel pipe. Transactions of the China Welding Institution 32(2):81–84

26. Ma J, Kong F, Kovacevic R (2012) Finite-element thermal analysis of laser welding of galvanized high-strength steel in a zero-gap lap joint configuration and its experimental verification. Mater Des 36: 348–358. doi:10.1016/j.matdes.2011.11.027
27. Kong F, Ma J, Kovacevic R (2011) Numerical and experimental study of thermally induced residual stress in the hybrid laser–GMA welding process. J Mater Process Technol 211(6):1102–1111. doi: 10.1016/j.jmatprotec.2011.01.012
28. Qi XD, Song G (2010) Interfacial structure of the joints between magnesium alloy and mild steel with nickel as interlayer by hybrid laser-TIG welding. Mater Des 31(1):605–609. doi:10.1016/j.matdes.2009.06.043
29. Depover T, Wallaert E, Verbeken K (2016) Fractographic analysis of the role of hydrogen diffusion on the hydrogen embrittlement susceptibility of DP steel. Mater Sci Eng A 649:201–208. doi:10.1016/j.msea.2015.09.124